Magnetotransport Properties of Layered Topological Material $ZrTe_2$ Thin Film

Huichao Wang[†,], Cheuk Ho Chan[†], Chun Hung Suen, Shu Ping Lau, and Ji-Yan Dai[*]*

Department of Applied Physics, The Hong Kong Polytechnic University, Hung Hom, Kowloon, Hong Kong, P. R. China

Corresponding Author: *Email: jiyan.dai@polyu.edu.hk; hcwang90@163.com.

ABSTRACT-$ZrTe_2$ is a candidate of topological materials from the layered two-dimensional transition-metal dichalcogenides family, and thus the material may show exotic electrical transport properties and be promising for quantum device applications. In this work, we report the successful growth of layered $ZrTe_2$ thin film by pulsed-laser deposition and the experimental results of its magnetotransport properties. In the presence of a perpendicular magnetic field, the 60 nm-thick $ZrTe_2$ film shows a large magnetoresistance of 3000% at 2 K and 9 T. A robust linear magnetoresistance is observed under an in-plane magnetic field, and negative magnetoresistance appears in the film when the magnetic field is parallel to the current direction. Furthermore, the Hall results reveal that the $ZrTe_2$ thin film has a high electron mobility of about 1.8×10^4 $cm^2V^{-1}s^{-1}$ at 2 K. These findings provide insights into further investigations and potential applications of this layered topological material system.

KEYWORDS: *$ZrTe_2$ thin film, topological material, pulsed-laser deposition, large magnetoresistance, linear magnetoresistance, high mobility*

ToC graphic:

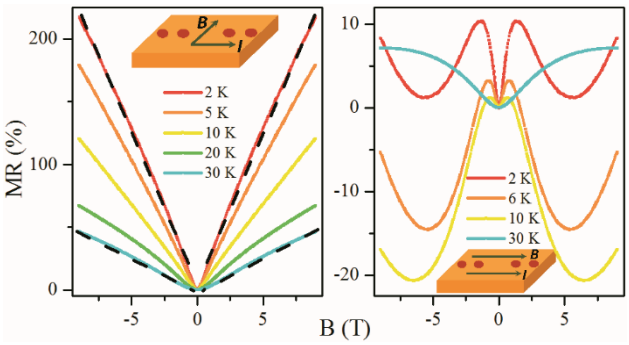

Layered transition-metal dichalcogenides (TMDs) have been one of the most extensively studied class of materials in recent years. The TMDs possess X-M-X layers with the transition metal atom M (Mo, W, Ta, Zr, Hf, *etc.*) sandwiched between two chalcogen atoms (X=S, Se or Te) and the layers are separated by the van der Waals gap, which offer new promising platforms beyond graphene for exploring striking phenomena and device applications.[1] In particular, with the development of topological materials, the TMDs with nontrivial topology have attracted great interests in the past decades because of their fascinating physical properties related to the Dirac cone in electronic band structures. The $MoTe_2$ and WTe_2 systems were theoretically considered to be type-II topological Weyl semimetals (WSM), in which the Weyl cones are titled and the Weyl fermion manifests Lorentz-violating behavior.[2,3] Later, the type-II WSM feature of $MoTe_2$ was confirmed by spectroscopic evidence from the angle-resolved photoemission spectroscopy (ARPES) results.[4-9] Furthermore, by electrical transport measurements, the $MoTe_2$ was found to be superconducting and nontrivial superconducting signatures were observed in the topological S-doped $MoTe_2$.[10-13] The semimetal WTe_2 possessing quite large magnetoresistance (MR) was also studied by using ARPES and spectroscopic evidences for the type-II WSM trait were provided.[14-16] Moreover, interesting magnetotransport effect associated with Weyl fermions, the significant anisotropic chiral anomaly, was also reported in WTe_2.[17,18] Besides, the $PtTe_2$ was identified to be a type-II Dirac semimetal (DSM) with titled Dirac nodes by the combination of ARPES measurements and first-principles calculations.[19]

Lately, increasing research interests have been paid to the zirconium-based chalcogenides, especially the topological zirconium telluride compounds with exotic physical properties. $ZrTe_5$ was initially studied for its resistivity anomaly, thermoelectric performance and quantum oscillations.[20-23] The recent theoretical prediction of its topological nature has further ignited intensive research work, which shows that $ZrTe_5$ is extremely sensitive to the cell volume and can manifest as a DSM, a strong topological insulator (TI) or a weak TI under variant crystal volumes.[24-36] The compound shows many interesting transport phenomena, in which some are quite alluring due to the association with massless Dirac fermions, such as the chiral magnetic effect,[25] nontrivial Berry phase,[27,28] and discrete scale invariance featured with log-periodic quantum oscillations.[29]

Theoretical calculations indicate that ZrTe possesses the three-fold fermionic quasiparticles, which come from the three-fold degenerate crossing points formed by the crossing of a double-degeneracy band and a non-degeneracy band.[37-39] The magnetotransport measurements of ZrTe single crystals reveal features such as high carrier mobility and light cyclotron effective mass.[40] Very recently, the TMD material $ZrTe_2$ was studied by ARPES showing features of massless Dirac fermions.[41] As a topological material candidate from the layered TMD family,[42-44] the $ZrTe_2$ may show attractive electrical transport phenomena and promising prospect for quantum devices applications. However, related investigations have not been presented yet. Thus, it is desirable to explore the magnetotransport properties of $ZrTe_2$.

In this work, we report the magnetotransport characterization of $ZrTe_2$ thin film, which shows highly anisotropic MR behavior. The $ZrTe_2$ thin film was grown by using a pulsed-laser deposition (PLD) system and structurally characterized by X-ray diffraction (XRD) measurements and transmission electron microscopy (TEM). Firstly, the two-dimensional (2D) nature of the magnetotransport in $ZrTe_2$ film was clearly revealed. In a perpendicular magnetic field, the film shows a large MR of about 3000% at 2 K and 9 T. The violation of the Kohler's law and the nonlinear Hall traces indicate the existence of more than one type of carriers in $ZrTe_2$. By using two-carrier model analysis, we find the electron mobility can be as large as 1.8×10^4 $cm^2V^{-1}s^{-1}$ at low temperature 2 K. Furthermore, a robust linear MR was observed in the film when the magnetic field is in-plane and negative MR appears when the magnetic field is parallel to the current direction. This work systematically reveals the magnetotransport properties of the layered topological material $ZrTe_2$, which may shed light on the further study of the system.

RESULTS AND DISCUSSIONS

Synthesis of $ZrTe_2$ Thin Films The investigated $ZrTe_2$ thin films in this work were grown on the (110) $SrTiO_3$ (STO) substrate by PLD technique. The Coherent Excimer Laser used in this experiment is krypton fluoride laser with wavelength equals to 248 nm. The target is the zirconium telluride compound with the ratio of Zr:Te = 1:5 and the base pressure for film deposition is $5.0\text{x}10^{-5}$ Pa. It is found that the $ZrTe_2$ thin films are

extremely unstable under ambient atmosphere, so aluminum nitride (AlN) capping layer was used to protect the thin films from the moisture and air. The AlN was deposited *in-situ* at 250 ℃ with a thickness of about 60 nm using PLD. Under this condition, the AlN is polycrystalline with grain size of a few nanometers. With this cap layer's protection, the properties of the $ZrTe_2$ thin films show nearly no change after exposing in air for one week, and even show no change after storing in vacuum with pressure of about 2 Pa for months.

Structural Characterization by XRD and TEM The $ZrTe_2$ adopts a stable 1T (trigonal) phase with octahedral coordination of metal atoms (space group P-3m1 (D_{3d})), as shown in Fig. 1A. Figure 1B shows the XRD results of the thin films grown at selected temperatures ranging from 450 ℃ to 550 ℃. The comparison of XRD pattern with standard data (JCPDS card 54-560) reveals that the relatively intense peaks correspond to (0001), (0002), (0003) and (0004) planes of $ZrTe_2$, respectively, indicating that the $ZrTe_2$ thin film on the (110) STO substrate has a preferred orientation along its *c*-axis. Besides, two weaker peaks can be observed at ~29.3 ° and ~60.4 ° corresponding to $(01\bar{1}1)$ and $(02\bar{2}2)$ planes of $ZrTe_2$, respectively. They reveal a secondary growth orientation of the $ZrTe_2$ thin film, which was confirmed by the following TEM examination. We find that the intensity ratio of $ZrTe_2$ (0001) to STO (110) is lower when the growth temperature is below 550 ℃, and the (0004) peak becomes almost invisible for the thin film grown at 450 ℃. This suggests the lower crystallinity for samples grown at lower growth temperatures. On the other hand, the peaks related to the *c*-axis oriented $ZrTe_2$ are absent in the XRD pattern for samples grown at temperatures higher than 550 ℃. These results indicate that the temperature window for growing good crystallinity of $ZrTe_2$ phase is around 550 ℃. Thus, our further study was focused on the $ZrTe_2$ film grown at 550 ℃.

To study the microstructure of the $ZrTe_2$ thin film, TEM characterization was carried out with the TEM samples prepared using focused ion beam. Figure 2A shows the low-magnification cross-sectional view of the $ZrTe_2$ film grown on (110) STO substrate at 550 ℃ and the corresponding high-resolution image is shown in Fig. 2B. The uniform contrast within the 60 nm-thick film suggests layered growth mechanism along the *c*-axis of $ZrTe_2$, yet micro-domains with size of about 30 nm and with different orientations can be identified which are responsible for the surface roughness. It can also be observed that

there is a 5 nm-thick interfacial layer presenting a different growth orientation. We propose the mechanism that, at the earlier stage of growth, the film tends to grow with $(01\bar{1}1)$ parallel to the STO (110) surface (tetragonal-on-tetragonal lattices); but after a critical thickness of about 5 nm, low-energy (0001) plane of $ZrTe_2$ supersedes $(01\bar{1}1)$ plane as the main growth direction, so the film becomes layered growth mode. This can be clearly seen in the diffraction pattern shown in Fig. 2C, where one can see that the dominant crystallographic orientation relationship is $(0001)_{ZrTe2}//(110)_{STO}$; the ring type spray diffraction spots suggest that the in-plane orientation is not unique. We also perform energy-dispersive X-ray (EDX) measurements on the TEM sample and the EDX spectrum (Fig. 2D) indicates a Zr:Te ratio of about 1:2.

Two-Dimensional Nature of Magnetotransport Properties The sheet resistance of the $ZrTe_2$ thin film as a function of temperature (2-300 K) is shown in Fig. 3A, where the upper inset is schematic structure for the magnetotransport measurements. One can see that the film exhibits a typical metallic behavior, *i.e.*, the resistance decreases when the temperature is decreased. The film shows a very large residual-resistance ratio (RRR=R(300 K)/R(2 K)=2756), which indicates high quality of the sample. Figure 3B shows the angular-dependence of MR at 2 K and 9 T when the sample is tilted in a way as shown in the inset. The orange curve is a $|\cos\theta|$ fitting, where θ is the angle between the magnetic field and the *c*-axis of the $ZrTe_2$ film. The theoretical fitting matches with the experimental data (the green curve), revealing a 2D transport feature. When θ is close to 90 ℃270 ° (B//E), there exists apparent deviation between the measured MR and the theory. This indicates the existence of other underlying effect in this material when the magnetic and electrical fields are parallel (details are in the following discussions on the negative MR at B//E). Figure 3C shows the MR of the thin film at selected values for the angle θ. Based on the measured data in Fig. 3C, the MR behavior as a function of the perpendicular magnetic field component $B_{\perp}$ is shown in Fig. 3D. It is apparent that the MR at different angles can be perfectly collapsed onto one single curve. These results demonstrate the 2D nature of the magnetotransport properties.[45]

Large MR effect, Violation of Kohler's Rule and Nonlinear Hall Traces Figure 4A shows the MR of the $ZrTe_2$ thin film at selected temperatures when the external magnetic

field is perpendicular to the film plane (B//*c*-axis). One can see a very large and non-saturating MR=(R(H)-R(0))/R(0)≈3000% when the sample is at 2 K and 9 T. As the temperature is increased to 10 K above, the MR sharply decreases. For a conventional metallic material, the MR at a certain temperature under a magnetic field obeys a general function known as Kohler's rule:[46]

$$\frac{\Delta\rho(T,B)}{\rho(T,0)} = F(\frac{B}{\rho(T,0)}) \ , \quad (1)$$

where *T* denotes temperature, *B* denotes magnetic field and ρ(T,0) denotes the zero-field resistivity. If the number of charge carriers is a constant and the scattering time is not significantly dependent on the location along the Fermi surface, the Kohler's rule can be hold and the MR measured at different temperatures is expected to collapse into a single temperature-independent curve. Figure 4B illustrates the Kohler plots of the measured MR of $ZrTe_2$ thin film in the perpendicular fields. Here we assume the function $F(B/\rho(T,0))=A(T)(B/\rho(T,0))^2$ with parameter *A*(T) due to the MR's parabolic dependence on the magnetic field. It is apparent that the Kohler's law does not hold for any range of temperatures or fields. The violation of such a rule means that the MR behavior in the $ZrTe_2$ thin film cannot be described in terms of semi-classical transport on a single Fermi surface with a single scattering time.[47,48]

To obtain detailed carrier information in the $ZrTe_2$ thin film, we also measured its Hall traces at different temperatures, and the results are shown in Fig. 4C. The nonlinear feature of the Hall behavior is obvious at low temperatures below 20 K and becomes weak at relatively higher temperatures. The nonlinear dependence of Hall behavior on the magnetic field clearly reveals the existence of more than one type of carriers in the sample, which is in agreement with the fact of violation of Kohler's law. We use a two-carrier model to analyze the carriers in the $ZrTe_2$ thin film with the following equation:[49]

$$\sigma_{xy} = \mathrm{eB}(\frac{n_1\mu_1^2}{1+\mu_1^2B^2} + \frac{n_2\mu_2^2}{1+\mu_2^2B^2}) \quad (2),$$

where the Hall conductivities σ_{xy} can be obtained with the measured ρ_{xx} and ρ_{yx}. Figure 4D shows the estimated carrier density and mobility as a function of temperature. The results

indicate that holes and electrons coexist in the film at low temperatures. As the temperature is increased, the density of hole carriers decreases and then two types of electrons contribute to the electrical transport above 30 K. The electrons show a high mobility of about 1.8×10^4 $cm^2V^{-1}s^{-1}$ at 2 K, suggesting the potential for promising electronic applications. Despite of the high mobility, quantum oscillations were not observed in this sample within the measured regime of magnetic field and temperature due to the quite large carrier concentration.

Linear MR Behavior at Parallel Magnetic Fields Figures 5A and 5B show the MR behavior when the in-plane magnetic field is perpendicular to the excitation current direction, where a non-saturating linear MR is apparent. At 2 K, the perfect linear MR even persists in the full magnetic field regime of 0-±9 T and the MR at ±9T is as large as 220%. When the temperature is increased, the MR behavior around the zero-field evolves to the classical parabolic dependence on the magnetic field; the linear MR survives at the large magnetic field regime without saturation. To understand the exotic linear MR, we further measured the angular dependence of the MR. As shown in Fig. 5C, the linear MR remains at quite a large angular (φ) regime, meaning that the linear behavior is not sensitive to the perpendicular configuration of the in-plane magnetic field and the current. When φ is close to 90 °(B//E), other underlying effect appears and may be responsible for the shape change of the MR curves (details are in the following discussions on the negative MR at B//E). The results reveal that there is a robust linear MR in the $ZrTe_2$ thin film, which remains in a wide range of temperatures and angles.

Negative MR at Parallel Magnetic and Electrical Fields As shown in Fig. 5C, negative MR behavior can be observed in the $ZrTe_2$ thin film when the magnetic and electrical fields are nearly parallel. Detailed angular dependence of the negative MR is shown in Fig. 6A. One can see that the negative MR is very sensitive to the relative orientation of the in-plane magnetic fields and the excitation current. The negative MR behavior when B//I at selected temperatures is shown in Fig. 6B, and we can find that the negative MR disappears at temperatures above 30 K. The positive MR behavior at low temperatures and large magnetic fields in Fig. 6B may come from the mismatch of the relative orientation of the in-plane magnetic field and the current.

Discussions of the Results Based on topological materials arsenal, the theoretical calculations predict that $ZrTe_2$ is a topological crystalline insulator (TCI) possessing metallic surface states protected by crystalline symmetry.[42-44] The surface conduction can induce a 2D feature in electron transport, just as what we observed in our experimental results shown in Figs. 3B and 3D. The 2D behavior alone does not necessarily indicate surface states since the origin may also arise from the anisotropic bulk transport in layered crystal structure or the band-bending generated two-dimensional electron gas.[50,51] However, our $ZrTe_2$ film also shows very large MR and high mobility at low temperatures with the coexistence of holes and electrons; in the TCI scenario the features may suggest contribution from surface states. The large carrier density in the $ZrTe_2$ thin film is hard to be understood then. And in addition, its MR (about 3000% at 2 K and 9 T) is at least an order of magnitude larger than those results of typical topological insulator.[52] The very large MR has now been observed in most of the topological semimetals such as Cd_3As_2, TaAs, and WTe_2, which usually also show high carrier concentration.[14,48,53-55] A recent ARPES study indicates that $ZrTe_2$ may be a three-dimensional DSM,[41] and this gives an alternative scenario to be responsible for our observations. The origin of the large MR effect in topological semimetals is still under debate, in which a possible mechanism may be from the compensation of the electron and hole pockets.[14,54,55] According to Figs. 4A and 4D, the large MR is apparent at low temperatures below 20 K when electrons and holes in the $ZrTe_2$ are nearly compensated. The MR effect quickly weakens when the temperature is further increased, and in this regime the compensation is gone. The consistent temperature dependence suggests that the large MR in $ZrTe_2$ thin film may be closely related to the compensation of electrons and holes.

For solid state materials under a magnetic field, linear MR is an unusual phenomenon in contrast to the usual semiclassical quadratic MR induced by the Lorentz force. The linear MR has been observed in a vast variety of materials including many topological materials, in which the reported linear MR was usually obvious in a perpendicular magnetic field.[56-63] Wide debates remain on the origin of linear MR in solids, which was ever suggested to be the Abrikosov's quantum linear MR, the novel linear dispersion, or the carrier fluctuation.[56-64] In our observation, the evident linear MR is robust under parallel magnetic fields surviving within a wide range of temperatures and angles. When the magnetic field

is perpendicular to the film plane, *i.e.*, along the stacking direction of layers, the MR shows non-saturating trend while the linear feature is not apparent. This suggests that the robust linear MR behavior in the $ZrTe_2$ thin film is closely related to the magnetic field applied to the 2D Te-Zr-Te layers. We estimate the carrier mobility from the parallel field MR around zero magnetic field, and the normalized linear MR and mobility are shown in Fig. 5D. The consistent behavior throughout the temperature range from 2 K to 100 K indicates that the linear MR is likely attributed to the carrier fluctuation in the $ZrTe_2$ thin film. [63,65]

Finally, there is a negative MR when the magnetic field is along the excitation current direction. The negative MR has been intensively studied recently in topological materials, which is ignited by the interesting concept called chiral magnetic effect or chiral (Adler-Bell-Jackiw) anomaly.[66,67] This effect arises from a charge pumping process between the Weyl nodes, which violates the conservation of chiral charges and leads to an axial charge current. This axial current gives rise to a negative MR behavior.[25] However, the observation of negative MR under E//B itself may not be a compelling signature of the chiral anomaly. Some basic explanations like the current jet effect or Berry curvature may equally be responsible for negative MR.[68-72] For example, similar negative MR at E//B without dependence on the crystal orientations was ever reported in TI films,[68] which was suggested to be attributed to a semi-classical framework considering the Berry curvature and orbital moment corrections but without chiral anomaly.[72] More related investigations would be helpful to clarify the origin of the negative MR behavior in the topological $ZrTe_2$.

CONCLUSION

In summary, magnetotransport properties of the topological material candidate $ZrTe_2$ have been systematically demonstrated. The $ZrTe_2$ indeed shows traits similar to those observed in most of typical topological materials, such as the large MR (~3000% at 2 K and 9 T) and the high electron mobility (1.8×10^4 $cm^2V^{-1}s^{-1}$ at 2 K). Furthermore, the $ZrTe_2$ thin film displays interesting anisotropic MR behavior with 2D nature. In particular, a large linear MR is robust in parallel magnetic fields and a negative MR appears closely related to the configuration of E//B. The high mobility and robust linear MR shows promise for

potential device applications. Our work may stimulate further theoretical and experimental studies on this layered topological material.

METHODS

A KrF laser (Lambda Physik COMPex 205) with the wavelength of 248 nm was used to focus on the zirconium telluride compound target. The energy density was set to be about 5 J mm^{-2} with a pulse frequency of 5 Hz. The STO (110) substrate was adjusted to be 6.5 cm away from the target and heated to 550ºC for $ZrTe_2$ film deposition. Subsequently, a capping layer of AlN was coated at 200ºC, and after that, the sample was cooled down to room temperature in vacuum naturally. The XRD results were taken using the Rigaku SmartLab and the TEM investigations were performed in a JEOL 2100F operating at 200 kV. The electrical transport measurements of the films were conducted in a 9T-PPMS (Physical Property Measurement System) from Quantum Design. For the results shown in the work, electrodes are all made by pressing indium with 25 μm diameter Al wires connected to the sample stage. The indium electrodes can punch through the cap layer by pressing.

ASSOCIATED CONTENT

The authors declare no competing financial interest.

AUTHOR INFORMATION

Corresponding Author

*Email: jiyan.dai@polyu.edu.hk.

*Email: hcwang90@163.com.

Author Contributions

†H. W. and C. H. C. contributed equally.

ACKNOWLEDGMENT

This research was supported by Hong Kong GRF grant (153094/16P). Financial support from The Hong Kong Polytechnic University strategic plan (No: 1-ZE25 and 1-ZVCG) and postdoc fellow scheme (1-YW0T).

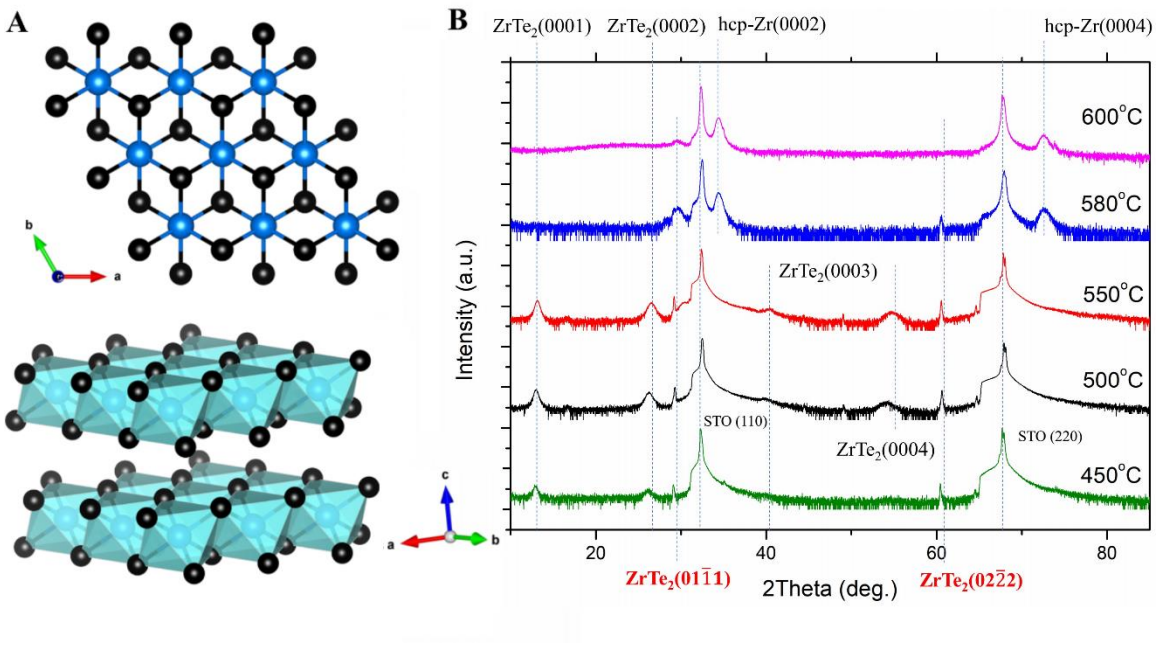

Figure 1. (A) Top and side views of $ZrTe_2$ crystal structure. The cross section shows the octahedral surroundings of the zirconium atom by the telluride atoms. (B) XRD results of the zirconium telluride thin films on STO (110) substrate grown at different temperatures.

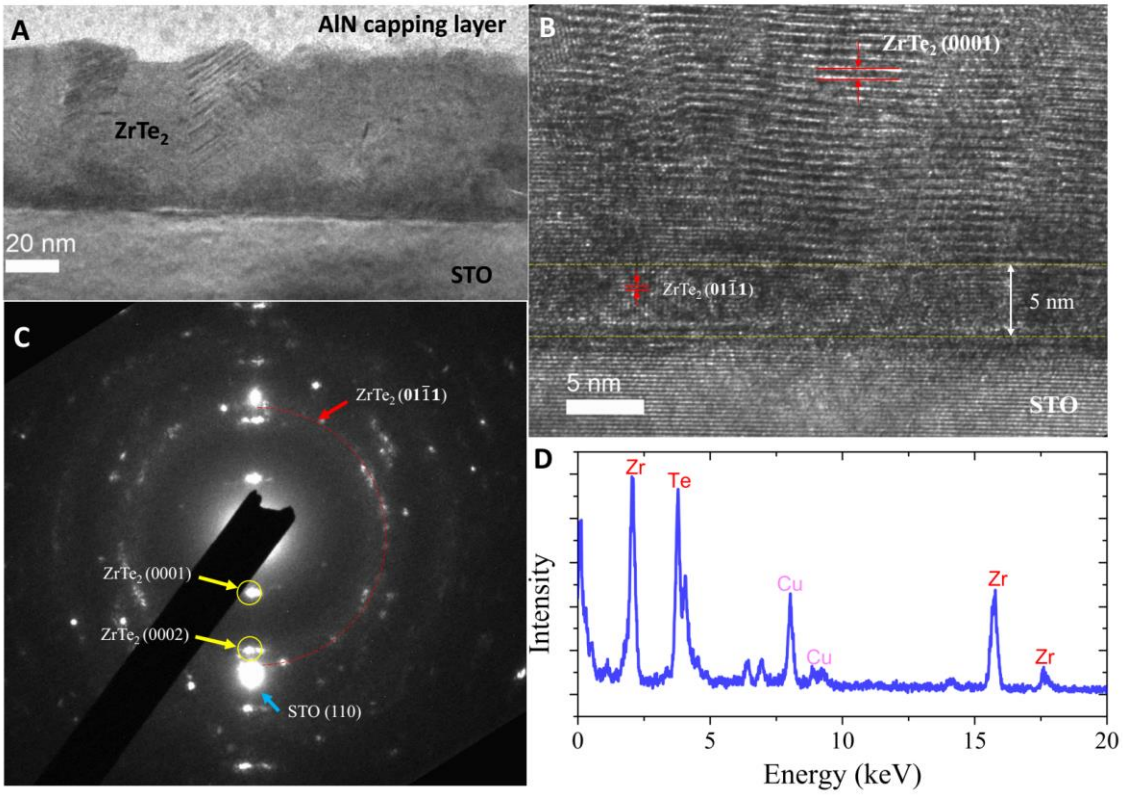

Figure 2. (A) The cross-section TEM image of the $ZrTe_2$ thin film grown on STO (110) at 550°C. (B) High-resolution TEM image showing the $ZrTe_2$ (0001) lattice indicating layered structure. The 5 nm thick interfacial layer suggests the $(01\bar{1}1)$ plane growth during the early stage of $ZrTe_2$ deposition. (C) The superimposed SAED pattern taken from both the film and substrate. (D) EDX spectrum showing Zr:Te ratio close to 1:2.

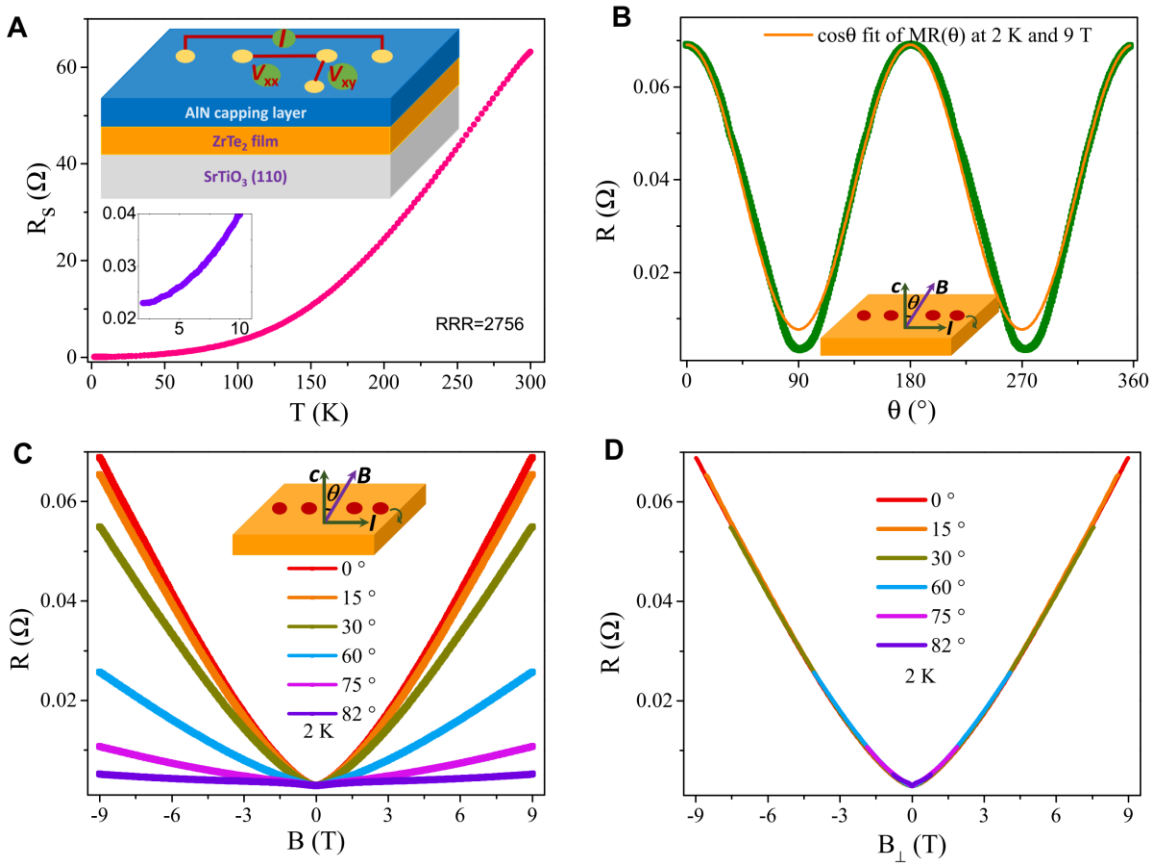

Figure 3. (A) Temperature dependence of the sheet resistance in the $ZrTe_2$ thin film. Upper inset: A schematic structure for the electrical transport measurements. Lower inset: Magnification of the results at low temperatures. (B) MR as a function of the tilted angle when the film sample is rotated as in the inset schema at T = 2 K and 9 T. The |cos θ| fitting is shown as an orange curve. (C) MR *vs.* magnetic field at selected angles θ. (D) MR *vs.* the perpendicular component of magnetic field Bcosθ. The angular dependence results reveal a 2D nature of the magnetotransport properties in $ZrTe_2$.

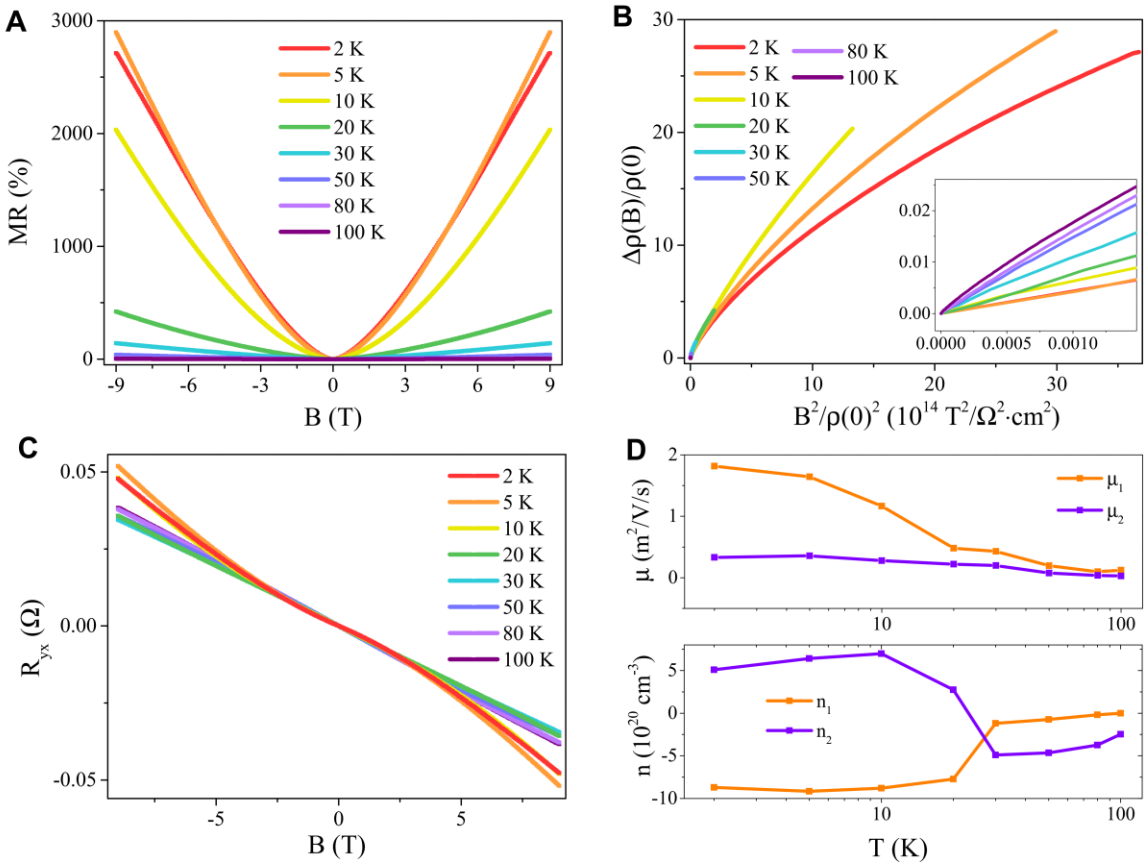

Figure 4. (A) MR of the $ZrTe_2$ thin film at selected temperatures measured in the perpendicular field with B // *c* axis. (B) Kohler plots for the MR at different temperatures from 2 to 100 K. The inset shows an enlargement. (C) Hall traces of the thin film. (D) Temperature dependence of the estimated carrier density and mobility in the $ZrTe_2$ thin film.

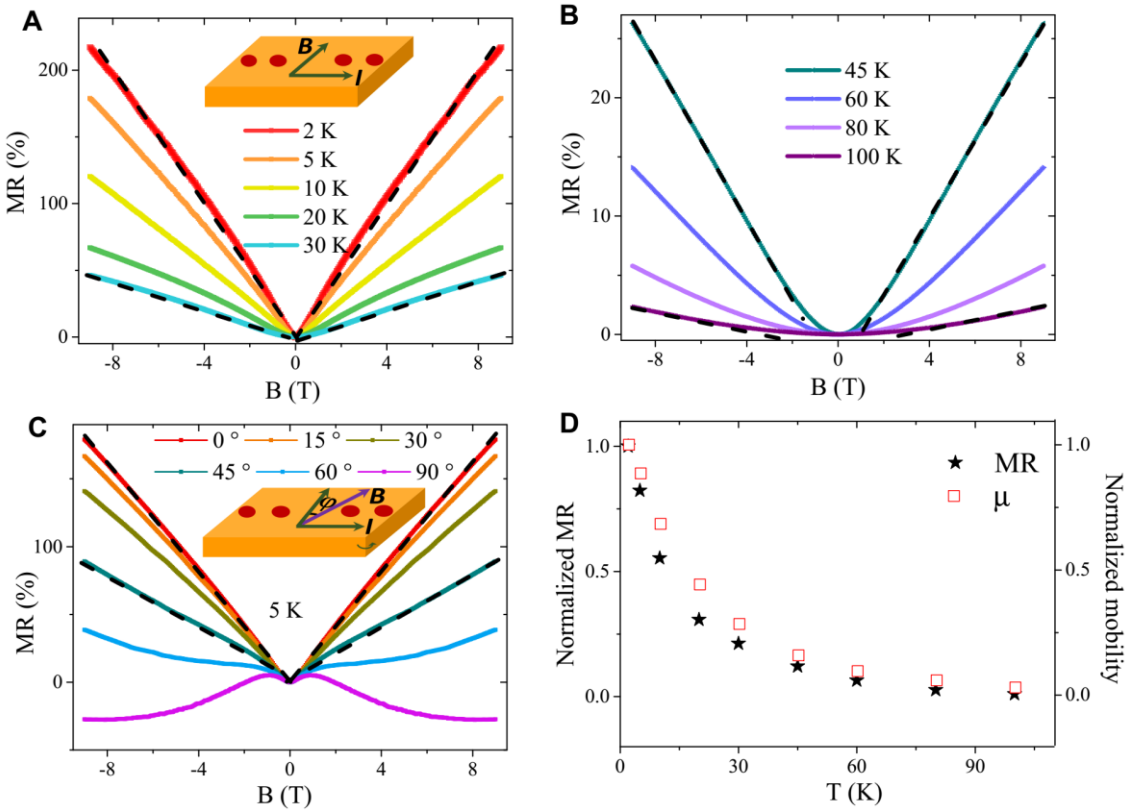

Figure 5. (A) and (B) Linear MR behavior in $ZrTe_2$ thin film at different temperatures when the in-plane magnetic field is perpendicular to the current direction. (C) Angular dependence of the linear MR when the sample is rotated as in the inset schema. (D) MR at 9T and estimated mobility from parallel magnetic field MR at different temperatures.

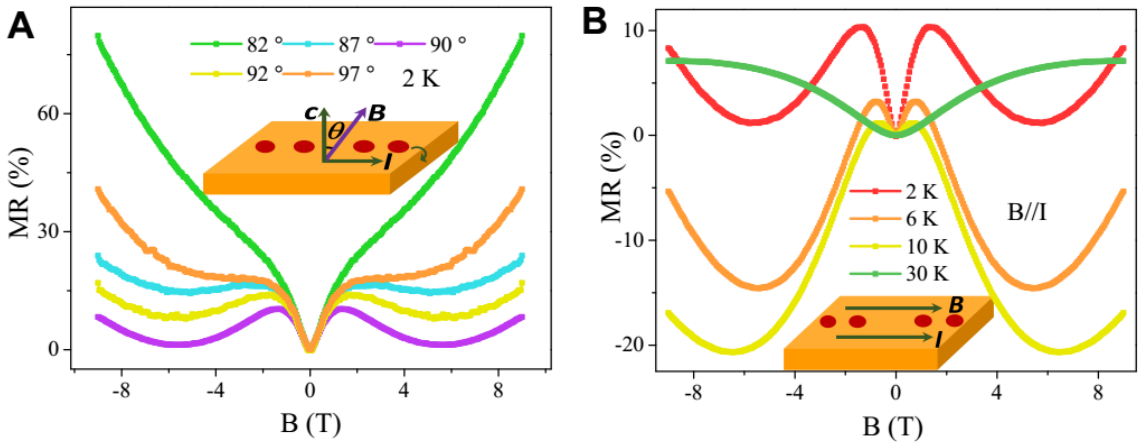

Figure 6. (A) Negative MR behavior in $ZrTe_2$ thin film when the magnetic and electric fields are nearly parallel. (B) Negative MR at selected temperatures.

References

(1) Manzeli, S.; Ovchinnikov, D.; Pasquier, D.; Yazyev, O. V.; Kis, A. 2D Transition Metal Dichalcogides. *Nat. Rev. Mater.* **2017**, 2, 17033.

(2) Chang, T. R.; Xu, S. Y.; Chang, G.; Lee, C. C.; Huang, S. M.; Wang, B.; Bian, G.; Zheng, H.; Sanchez, D. S.; Belopolski, I.; Alidoust, N.; Neupane, M.; Bansil, A.; Jeng, H. T.; Lin, H.; Hasan, M. Z. Prediction of an Arc-Tunable Weyl Fermion Metallic State in $Mo_xW_{1-x}Te_2$. *Nat*. *Commun*. **2016**, 7, 10639.

(3) Sun, Y.; Wu, S. C.; Ali, M. N.; Felser, C.; Yan, B. Prediction of Weyl Semimetal in Orthorhombic $MoTe_2$. *Phys*. *Rev*. *B* **2015**, 92, 161107(R).

(4) Wang, Z.; Gresch, D.; Soluyanov, A. A.; Xie, W.; Kushwaha, S.; Dai, X.; Troyer, M.; Cava, R. J.; Bernevig, B. A. $MoTe_2$: A Type-II Weyl Topological Metal. *Phys*. *Rev*. *Lett*. **2016**, 117, 056805.

(5) Deng, K.; Wan, G.; Deng, P.; Zhang, K.; Ding, S.; Wang, E.; Yan, M.; Huang, H.; Zhang, H.; Xu, Z.; Denlinger, J.; Fedorov, A.; Yang, H.; Duan, W.; Yao, H.; Wu, Y.; Fan, S.; Zhang, H.; Chen, X.; Zhou, S. Experimental Observation of Topological Fermi Arcs in Type-II Weyl Semimetal $MoTe_2$. *Nat*. *Phys*. 2016, 12, 1105-1110.

(6) Huang, L.; McCormick, T. M.; Ochi, M.; Zhao, Z.; Suzuki, M. T.; Arita, R.; Wu, Y.; Mou, D.; Cao, H.; Yan, J.; Trivedi, N.; Kaminski, A. Spectroscopic Evidence for a Type II Weyl Semimetallic State in $MoTe_2$. *Nat*. *Mater*. **2016**, 15, 1155-1160.

(7) Tamai, A.; Wu, Q. S.; Cucchi, I.; Bruno, F. Y.; Ricco, S.; Kim, T. K.; Hoesch, M.; Barreteau, C.; Giannini, E.; Besnard, C.; Soluyanov, A. A.; Baumberger, F. Fermi Arcs and Their Topological Character in the Candidate Type-II Weyl Semimetal $MoTe_2$. *Phys*. *Rev*. *X* **2016**, 6, 031021.

(8) Liang, A.; Huang, J.; Nie, S.; Ding, Y.; Gao, Q.; Hu, C.; He, S.; Zhang, Y.; Wang, C.; Shen B.; Liu, J.; Ai, P.; Yu, L.; Sun, X.; Zhao, W.; Lv, S.; Liu, D.; Li, C.; Zhang, Y.; Hu, Y.; *et al.* Electronic Evidence for Type II Weyl Semimetal State in $MoTe_2$. *arXiv*:1604.01706.

(9) Jiang, J.; Liu, Z. K.; Sun, Y.; Yang, H. F.; Rajamathi, C. R.; Qi, Y. P.; Yang, L. X.; Chen, C.; Peng, H.; Hwang, C. C.; Sun, S. Z.; Mo, S. K.; Vobornik, I.; Fujii, J.; Parkin, S. S. P.; Felser, C.; Yan, B. H.; Chen, Y. L. Signature of Type-II Weyl Semimetal Phase in $MoTe_2$. *Nat*. *Commun*. **2017**, 8, 13973.

(10) Qi, Y.; Naumov, P. G.; Ali, M. N.; Rajamathi, C. R.; Schnelle, W.; Barkalov, O.; Hanfland, M.; Wu, S. C.; Shekhar, C.; Sun, Y.; Süß, V.; Schmidt, M.; Schwarz, U.; Pippel, E.; Werner, P.; Hillebrand, R.; Förster, T.; Kampert, E.; Parkin, S.; Cava, R. J.; *et al.* Superconductivity in Weyl Semimetal Candidate $MoTe_2$. *Nat. Commun.* **2016**, 7, 11038.

(11) Chen, F. C.; Luo, X.; Xiao, R. C.; Lu, W. J.; Zhang, B.; Yang, H. X.; Li, J. Q.; Pei, Q. L.; Shao, D. F.; Zhang, R. R.; Ling, L. S.; Xi, C. Y.; Song, W. H.; Sun, Y. P. Superconductivity Enhancement in the S-Doped Weyl Semimetal Candidate $MoTe_2$. *Appl. Phys. Lett.* **2016**, 108, 162601.

(12) Li, Y. N.; Gu, Q. Q.; Chen, C.; Zhang, J.; Liu, Q.; Hu, X. Y.; Liu, J.; Liu, Y.; Ling, L. S.; Tian, M. L.; Wang, Y.; Samarth, N.; Li, S. Y.; Zhang, T.; Feng, J.; Wang, J. Nontrivial Superconductivity in Topological $MoTe_{2-x}S_x$ Crystals. *PNAS*, **2018**, 115, 9503-9508.

(13) Guguchia, Z.; Rohr, F.; Shermadini, Z.; Lee, A. T.; Banerjee, S.; Wieteska, A. R.; Marianetti, C. A.; Frandsen, B. A.; Luetkens, H.; Gong, Z.; Cheung, S. C.; Baines, C.; Shengelaya, A.; Taniashvili, G.; Pasupathy, A. N.; Morenzoni, E.; Billinge, S. J. L.; Amato, A.; Cava, R. J.; Khasanov, R.; *et al.* Signatures of the Topological s+- Superconducting Order Parameter in the Type-II Weyl Semimetal T_d-$MoTe_2$. *Nat. Commun.* **2017**, 8, 1082.

(14) Ali, M. N.; Xiong, J.; Flynn, S.; Tao, J.; Gibson, Q. D.; Schoop, L. M.; Liang, T.; Haldolaarachchige, N.; Hirschberger, M.; Ong, N. P.; Cava, R. J. Large, Non-Saturating Magnetoresistance in WTe_2. *Nature* **2014**, 514, 205-208.

(15) Soluyanov, A. A.; Gresch, D.; Wang, Z.; Wu, Q.; Troyer, M.; Dai, X.; Bernevig, B. A. Type-II Weyl Semimetals. *Nature* **2015**, 527, 495-498.

(16) Wang, C.; Zhang, Y.; Huang, J.; Nie, S.; Liu, G.; Liang, A.; Zhang, Y.; Sehen, B.; Liu, J.; Hu, C.; Ding, Y.; Liu, D.; Hu, Y.; He, S.; Zhao, L.; Yu, L.; Hu, J.; Wei, J.; Mao, Z.; Shi, Y.; *et al.* Observation of Fermi Arc and Its Connection with Bulk States in the Candidate Type-II Weyl Semimetal WTe_2. *Phys. Rev. B* **2016**, 94, 241119(R).

(17) Wang, Y.; Liu, E.; Liu, H.; Pan, Y.; Zhang, L.; Zeng, J.; Fu, Y.; Wang, M.; Xu, K.; Huang, Z.; Wang, Z.; Lu, H. Z.; Xing, D.; Wang, B.; Wan, X.; Miao, F. Gate-Tunable Negative Longitudinal Magnetoresistance in the Predicted Type-II Weyl Semimetal WTe_2. *Nat. Commun.* **2016**, 7, 13142.

(18) Lv, Y. Y.; Li X.; Zhang, B. B.; Deng, W. Y.; Yao, S. H.; Chen, Y. B.; Zhou, J.; Zhang, S. T.; Lu, M. H.; Zhang, L.; Tian, M.; Sheng, L.; Chen, Y. F. Experimental Observation of Anisotropic Adler-Bell-Jackiw Anomaly in Type-II Weyl Semimetal $WTe_{1.98}$ Crystals at the Quasiclassical Regime. *Phys*. *Rev*. *Lett*. **2017**, 118, 096603.

(19) Yan, M.; Huang, H.; Zhang, K.; Wang, E.; Yao, W.; Deng, K.; Wan, G.; Zhang, H.; Arita, M.; Yang, H.; Sun, Z.; Yao, H.; Wu, Y.; Fan, S.; Duan, W.; Zhou, S. Lorentz-Violating Type-II Dirac Fermions in Transition Metal Dichalcogenide $PtTe_2$. *Nat*. *Commun*. **2017**, 8, 257.

(20) Okada, S.; Sambongi, T.; Ido, M. Giant Resistivity Anomaly in $ZrTe_5$. *J. Phys. Soc. Jpn.* **1980**, 49, 839-840.

(21) Shaviv, R.; Westrum, E. F.; Fjellvåg, H.; Kjekshus, A. $ZrTe_5$ and $HfTe_5$: The Heat Capacity and Derived Thermophysical Properties from 6 to 350 K. *J. Solid State Chem.* **1989**, 81, 103-111.

(22) Kamm, G. N.; Gillespie, D. J.; Ehrlich, A. C.; Wieting, T. J.; Levy, F. Fermi Surface, Effective Masses, and Dingle Temperatures of $ZrTe_5$ as Derived from the Shubnikov–de Haas Effect, *Phys*. *Rev*. *B* **1985**, 31, 7617.

(23) Izumi, M.; Nakayama, T.; Uchinokura, K.; Harada, S.; Yoshizaki, R.; Matsuura, E. Shubnikov-de Haas Oscillations and Fermi Surfaces in Transition-Metal Pentatellurides $ZrTe_5$ and $HfTe_5$. *J. Phys. C: Solid State Phys*. **1987**, 20, 3691-3705.

(24) Weng, H.; Dai, X.; Fang, Z. Transition-Metal Pentatelluride $ZrTe_5$ and $HfTe_5$: A Paradigm for Large-Gap Quantum Spin Hall Insulators. *Phys. Rev. X* 2014, 4, 011002.

(25) Li, Q.; Kharzeev, D. E.; Zhang, C.; Huang, Y.; Pletikosic, I.; Fedorov, A. V.; Zhong, R. D.; Schneeloch, J. A.; Gu, G. D.; Valla, T. Chiral Magnetic Effect in $ZrTe_5$. *Nat*. *Phys*. **2016**, 12, 550-554.

(26) Chen, R. Y.; Chen, Z. G.; Song, X. Y.; Schneeloch, J. A.; Gu, G. D.; Wang, F.; Wang, N. L. Magnetoinfrared Spectroscopy of Landau Levels and Zeeman Splitting of Three-Dimensional Massless Dirac Fermions in $ZrTe_5$. *Phys*. *Rev*. *Lett*. **2015**, 115, 176404.

(27) Zheng, G.; Lu, J.; Zhu, X.; Ning, W.; Han, Y.; Zhang, H.; Zhang, J.; Xi, C.; Yang, J.; Du, H.; Yang, K.; Zhang, Y.; Tian, M. Transport Evidence for the Three-Dimensional Dirac Semimetal Phase in $ZrTe_5$. *Phys*. *Rev*. *B* **2016**, 93, 115414.

(28) Liu, Y.; Yuan, X.; Zhang, C.; Jin, Z.; Narayan, A.; Luo, C.; Chen, Z.; Yang, L.; Zou, J.; Wu, X.; Sanvito, S.; Xia, Z.; Li, L.; Wang, Z.; Xiu, F. Zeeman Splitting and Dynamical Mass Generation in Dirac Semimetal $ZrTe_5$. *Nat. Commun*. **2016**, 7, 12516.

(29) Wang, H. C.; Liu, H. W.; Li, Y. N.; Liu, Y. J.; Wang, J. F.; Liu, J.; Dai, J. Y.; Wang, Y.; Li, L.; Yan, J. Q.; Mandrus, D.; Xie, X. C. Wang, J. Discovery of Log-Periodic Oscillations in Ultraquantum Topological Materials. *Sci. Adv.* **2018**, 4, eaau5096.

(30) Li, X. B.; Huang, W. K.; Lv, Y. Y.; Zhang, K. W.; Yang, C. L.; Zhang, B. B.; Chen, Y. B.; Yao, S. H.; Zhou, J.; Lu, M. H.; Sheng, L.; Li. S. C.; Jia, J. F.; Xue, Q. K.; Chen, Y. F.; Xing, D. Y. Experimental Observation of Topological Edge States at the Surface Step Edge of the Topological Insulator $ZrTe_5$. *Phys. Rev. Lett*. **2016**, 116, 176803.

(31) Wu, R.; Ma, J. Z.; Nie, S. M.; Zhao, L. X.; Huang, X.; Yin, J. X.; Fu, B. B.; Richard, P.; Chen, G. F.; Fang, Z.; Dai, X.; Weng, H. M.; Qian, T.; Ding, H.; Pan, S. H. Evidence for Topological Edge States in a Large Energy Gap near the Step Edges on the Surface of $ZrTe_5$. *Phys. Rev. X* **2016**, 6, 021017.

(32) Zhang, Y.; Wang, C.; Yu, L.; Liu, G.; Liang, A.; Huang J.; Nie, S.; Sun, X.; Zang, Y.; Shen, B.; Liu, J.; Weng, H.; Zhao, L.; Chen, G.; Jia, X.; Hu, C.; Ding, Y.; Zhao, W.; Gao, Q.; Li, C.; *et al.* Electronic Evidence of Temperature-Induced Lifshitz Transition and Topological Nature in $ZrTe_5$. *Nat. Commun.* **2017**, 8, 15512.

(33) Manzoni, G.; Gragnaniello, L.; Autès, G.; Kuhn, T.; Sterzi, A.; Cilento, F.; Zacchigna, M.; Enenkel, V.; Vobornik, I.; Barba, L.; Bisti, F.; Bugnon, P.; Magrez, A.; Strocov, VN.; Berger, H.; Yazyev, OV.; Fonin, M.; Parmigiani, F.; Crepaldi, A. Evidence for a Strong Topological Insulator Phase in $ZrTe_5$. *Phys. Rev. Lett*. 2016, **117**, 237601.

(34) Jiang, Y.; Dun, Z. L.; Zhou, H. D.; Lu, Z.; Chen, K. W.; Moon, S.; Besara, T.; Siegrist, T. M.; Baumbach, R. E.; Smirnov, D.; Jiang, Z. Landau-Level Spectroscopy of Massive Dirac Fermions in Single-Crystalline $ZrTe_5$ Thin Flakes. *Phys. Rev. B* **2017**, 96, 041101.

(35) Fan, Z.; Liang, Q. F.; Chen, Y. B.; Yao, S. H.; Zhou, J. Transition between Strong and Weak Topological Insulator in $ZrTe_5$ and $HfTe_5$. Sci. Rep. **2017**, 7, 45667.

(36) Wang, H. C.; Wang, J. Electron Transport in Dirac and Weyl Semimetals. *Chinese Physics B* **2018**, 27, 107402.

(37) Zhu, Z.; G. Winkler, W.; Wu, Q.; Li, J.; Soluyanov, A. A. Triple Point Topological Metals. *Phys. Rev. X* **2016**, 6. 031003.

(38) Chang, G.; Xu, S.-Y.; Huang, S.-M.; Sanchez, D. S.; Hsu, C.-H.; Bian, G.; Yu, Z.-M.; Belopolski, I.; Alidoust, N.; Zheng, H.; Chang T.-R.; Jeng, H.-T.; Yang S. A.; Neupert, T.; Lin, H.; Hasan, M. Z. New Fermions on the Line in Topological Symmorphic Metals. *Sci. Rep.* **2017**, 7, 1688.

(39) Weng, H.; Fang, C.; Fang, Z.; Dai, X. Coexistence of Weyl Fermion and Massless Triply Degenerate Nodal Points. *Phys. Rev. B* **2016**, 94, 165201.

(40) Zhu, W. L.; He, J. B.; Zhang, S.; Chen, D.; Shan, L.; Ren, Z. A.; Chen, G. F.; Magnetotransport Properties of the New-Type Topological Semimetal ZrTe. *arXiv*:1707.00942.

(41) Tsipas, P.; Tsoutsou, D.; Fragkos, S.; Sant, R.; Alvarez, C.; Okuno, H.; Renaud, G.; Alcotte, R.; Baron, T.; Dimoulas, A. Massless Dirac Fermions in $ZrTe_2$ Semimetal Grown on InAs (111) by Van Der Waals Epitaxy. *ACS Nano* **2018**, 12, 1696-1703.

(42) Zhang, T.; Jiang, Y.; Song, Z.; Huang, H.; He, Y.; Fang, Z.; Weng H.; Fang, C. Catalogue of Topological Electronic Materials. *Nature* **2019**, 566, 475–479.

(43) Tang, F.; Po, H. C.; Vishwanath, A.; Wan, X. Comprehensive Search for Topological Materials Using Symmetry Indicators. *Nature* **2019**, 566, 486–489.

(44) Vergniory, M. G.; Elcoro, L.; Felser, C.; Regnault, N.; Bernevig B. A.; Wang. Z. A Complete Catalogue of High-Quality Topological Materials. *Nature* **2019**,566, 480-485.

(45) Zhao, Y.; Chang C. Z.; Jiang, Y.; DaSilva, A.; Sun, Y.; Wang, H.; Xing, Y.; Wang, Y.; He, K.; Ma, X.; Xue, Q. K.; Wang, J. Demonstration of Surface Transport in a Hybrid Bi_2Se_3/Bi_2Te_3 Heterostructure. *Sci*. *Rep*. **2013**, 3, 3060.

(46) Ziman, J. M. Electrons and Phonons: The Theory of Transport Phenomena in Solids. Clarendon, Oxford, UK, **2001**.

(47) McKenzie, R. H.; Qualls, J. S.; Han, S. Y.; Brooks, J. S. Violation of Kohler's Rule by the Magnetoresistance of a Quasi-Two-Timensional Organic Metal. *Phys*. *Rev*. *B* **1998**, 57, 11854.

(48) Zhao, Y. F.; Liu, H. W.; Yan, J. Q.; An, W.; Liu, J.; Zhang, X.; Wang, H. C.; Liu, Y.; Jiang, H.; Li, Q.; Wang, Y.; Li, X. Z.; Mandrus, D.; Xie. X. C.; Pan, M. H.; Wang, J.

Anisotropic Magnetotransport and Exotic Longitudinal Linear Magnetoresistance in WTe_2 Crystals. *Phys. Rev. B* **2015**, 92, 041104.

(49) Hurd, C. M. The Hall Effect in Metals and Alloys. Cambridge University Press, **1972**.

(50) Cao, H.; Tian, J.; Miotkowski, I.; Shen, T.; Hu, J.; Qiao, S.; Chen, Y. P. Quantized Hall Effect and Shubnikov–de Haas Oscillations in Highly Doped Bi_2Se_3: Evidence for Layered Transport of Bulk Carriers. *Phys. Rev. Lett.* **2012**, 108, 216803.

(51) Wang, J.; DaSilva, A. M.; Chang, C. Z.; He, K.; Jain, J. K.; Samarth, N.; Ma, X. C.; Xue, Q. K.; Chan, M. H. W. Evidence for Electron–Electron Interaction in Topological Insulator Thin Films. *Phys. Rev. B* **2011**, 83, 245438.

(52) Yan, Y.; Wang, L. X.; Yu, D. P.; Liao, Z. M. Large Magnetoresistance in High Mobility Topological Insulator Bi_2Se_3. *Appl. Phys. Lett.* **2013**, 103, 033106.

(53) Liang, T.; Gibson, Q.; Ali, M. N.; Liu, M.; Cava, R. J.; Ong, N. P. Ultrahigh Mobility and Giant Magnetoresistance in the Dirac Semimetal Cd_3As_2. *Nat. Mater.* **2015**, 14, 280-284.

(54) Zhang, C. L.; Yuan, Z.; Jiang, Q. D.; Tong, B.; Zhang, C.; Xie, X. C.; Jia, S. Electron Scattering in Tantalum Monoarsenide. *Phys. Rev. B* **2017**, 95, 085202.

(55) Huang, X.; Zhao, L.; Long, Y.; Wang, P.; Chen, D.; Yang, Z.; Liang, H.; Xue, M.; Weng, H.; Fang, Z.; Dai, X.; Chen, G. Observation of the Chiral-Anomaly-Induced Negative Magnetoresistance in 3D Weyl Semimetal TaAs. *Phys. Rev. X* **2015**, 5, 031023.

(56) Xu, R.; Husmann, A.; Rosenbaum, T. F.; Saboungi, M.-L.; Enderby, J. E.; Littlewood P. B. Large Magnetoresistance in Non-Magnetic Silver Chalcogenides. *Nature* **1997**, 390, 57-60.

(57) Friedman, A. L.; Tedesco, J. L.; Campbell, P. M.; Culbertson, J. C.; Aifer, E.; Perkins, F. K.; Myers-Ward, R. L.; Hite, J. K.; Eddy Jr., C. R., Jernigan, G. G.; Gaskill, D. K. Quantum Linear Magnetoresistance in Multilayer Epitaxial Graphene. *Nano Lett.* **2010**, 10, 3962-3965.

(58) Tang, H.; Liang, D.; Qiu, R. L.; Gao, X. P. Two-Dimensional Transport-Induced Linear Magneto-Resistance in Topological Insulator Bi_2Se_3 Nanoribbons. *ACS Nano* **2011**, 5(9), 7510-7516.

(59) Wang, X.; Du, Y.; Dou, S.; Zhang, C. Room Temperature Giant and Linear Magnetoresistance in Topological Insulator Bi_2Te_3 Nanosheets. *Phys*. *Rev*. *Lett*. **2012**, 108, 266806.

(60) He, L. P.; Hong, X. C.; Dong, J. K.; Pan, J.; Zhang, Z.; Zhang, J.; Li, S. Y. Quantum Transport Evidence for the Three-Dimensional Dirac Semimetal Phase in Cd_3As_2. *Phys*. *Rev*. *Lett*. **2014**, 113, 246402.

(61) Zhao, Y. F.; Liu, H. W.; Zhang, C. L.; Wang, H. C.; Wang, J. F.; Liu, Z. Q.; Xing, Y.; Lu, H.; Liu, J.; Wang, Y.; Brombosz, S. M.; Xiao, Z. L.; Jia, S.; Xie, X. C.; Wang, J. Anisotropic Fermi Surface and Quantum Limit Transport in High Mobility Three-Dimensional Dirac Semimetal Cd_3As_2. *Phys*. *Rev*. *X* **2015**, 5, 031037.

(62) Feng, J.; Pang, Y.; Wu, D.; Wang, Z.; Weng, H.; Li, J.; Dai, X.; Fang, Z.; Shi, Y.; Lu, L. Large Linear Magnetoresistance in Dirac Semimetal Cd_3As_2 with Fermi Surfaces Close to the Dirac Points. *Phys*. *Rev*. *B* **2015**, 92, 081306.

(63) Narayanan, A.; Watson, M. D.; Blake, S. F.; Bruyant, N.; Drigo, L.; Chen, Y. L.; Prabhakaran, D.; Yan, B.; Felser, C.; Kong, T.; Canfield, P. C.; Coldea, A. I. Linear Magnetoresistance Caused by Mobility Fluctuations in *n*-Doped Cd_3As_2. *Phys*. *Rev*. *Lett*. **2015**, 114, 117201.

(64) Abrikosov, A. A. Quantum Magnetoresistance. *Phys. Rev. B* **1998**, 58, 2788.

(65) Wang, Q.; Zhang, W.; Chen, W.; Xing, Y.; Sun, Y.; Wang, Z.; Mei, J.; Wang, Z.; Wang, L. L.; Ma, X. C.; Liu, F.; Xue Q. K.; and Wang, J. Spin Fluctuation Induced Linear Magnetoresistance in Ultrathin Superconducting FeSe Films. *2D Materials* **2017**, 4, 034004.

(66) Son, D. T.; Spivak, B. Z. Chiral Anomaly and Classical Negative Magnetoresistance of Weyl Metals. *Phys. Rev. B* **2013**, 88, 104412.

(67) Burkov, A. A. Chiral Anomaly and Transport in Weyl Metals. *J. Phys*. *Condens*. *Matt*. **2015**, 27, 113201.

(68) Wang, J.; Li, H.; Chang, C.; He, K.; Lee, J. S.; Lu, H.; Sun, Y.; Ma, X.; Samarth, N.; Shen, S.; Xue, Q. K.; Xie, M. H.; Chan, M. H. W. Anomalous Anisotropic Magnetoresistance in Topological Insulator Films. *Nano Res*. **2012**, 5, 739-746.

(69) Arnold, F.; Shekhar, C.; Wu, S. C.; Sun, Y.; Dos, Reis. R. D.; Kumar, N.; Naumann, M.; Ajeesh, M. O.; Schmidt, M.; Grushin, A. G.; Bardarson, J. H.; Baenitz, M.; Sokolov,

D.; Borrmann, H.; Nicklas, M.; Felser, C.; Hassinger, E.; Yan, B. Negative Magnetoresistance without Well-Defined Chirality in the Weyl Semimetal TaP. *Nat. Commun*. **2016**, 7, 11615.

(70) Lu, H. Z.; Shen, S. Q. Quantum Transport in Topological Semimetals under Magnetic Fields. *Front. Phys*. **2017**, 123, 127201.

(71) Andreev, A. V.; Spivak, B. Z. Longitudinal Negative Magnetoresistance and Magnetotransport Phenomena in Conventional and Topological Conductors. *Phys. Rev. Lett*. **2018**, 120, 026601.

(72) Dai, X.; Du, Z. Z.; Lu, H. Z. Negative Magnetoresistance without Chiral Anomaly in Topological Insulators. *Phys. Rev. Lett*. **2017**, 119, 166601.